

1 **Transient ionospheric upflow driven by poleward**
2 **moving auroral forms observed during the Rocket**
3 **Experiment for Neutral Upwelling 2 (RENU2)**
4 **campaign**

5 **M. Burleigh^{1,2}, M. Zettergren², K. Lynch³, M. Lessard⁴, J. Moen^{5,6}, L.**
6 **Clausen⁵, D. Kenward⁴, D. Hysell⁷, and M. Liemohn¹**

7 ¹University of Michigan
8 ²Embry-Riddle Aeronautical University
9 ³Dartmouth College
10 ⁴University of New Hampshire
11 ⁵University of Oslo
12 ⁶University Centre in Svalbard
13 ⁷Cornell University

14 **Key Points:**

15 • Imager data provides realistic transient forcing constraints for model inputs to sim-
16 ulate observations from a high-latitude rocket flight
17 • Transient forcing deposits energy over a wider latitudinal region but less energy
18 in any specific location
19 • Modeling a sequence of poleward moving auroral forms with realistic spatiotem-
20 poral variability generates significant latitudinal structuring

21 **Abstract**

22 This study examines cumulative effects of a series of poleward moving auroral forms (PMAFs)
 23 on ion upflow and downflow. These effects are investigated using an ionospheric model
 24 with inputs derived from the Rocket Experiment for Neutral Upwelling 2 (RENU2) sound-
 25 ing rocket campaign. Auroral precipitation inputs are constrained by all-sky imager bright-
 26 ness values resulting in significant latitudinal structuring in simulated ionospheric up-
 27 flows due to transient forcing. For contrast, a case with steady forcing, generates almost
 28 double the O^+ upflow transport through 1000 km when compared to PMAF-like struc-
 29 tures. At high altitudes, model results show a spread in upflow response time dependent
 30 on ion mass, with molecular ions responding slower than atomic ions by several minutes.
 31 While the modeled auroral precipitation is not strong enough to accelerate ions to es-
 32 cape velocities, source populations available for higher-altitude energization processes
 33 are greatly impacted by variable forcing exhibited by the RENU2 event.

34 **1 Introduction**

35 Heavy ions of ionospheric origin (e.g. O^+) are found throughout the terrestrial mag-
 36 netosphere (see reviews by Welling et al., 2015; Moore & Horwitz, 2007; Chappell, 1988).
 37 The presence of these ions in the magnetosphere results in mass-loading, variations in
 38 Alfvén speeds, and alteration of magnetic reconnection rate (e.g. Shay et al., 2004). Such
 39 alterations can have significant effects on the global magnetospheric behavior (e.g. Moore
 40 & Delcourt, 1995; Moore et al., 2005). Heavy ions are a significant component of the plas-
 41 masheet and ring current plasma, particularly during geomagnetically active times (Young
 42 et al., 1982; Kozyra et al., 1987; Gloeckler & Hamilton, 1987; Hamilton et al., 1988; Orsini
 43 et al., 1990; Nosé et al., 2005; Kistler et al., 2005). The cusp region is a prolific source
 44 of ionospheric outflow owing to its unique energy inputs (e.g. Varney et al., 2016; Hultqvist
 45 et al., 1999). Direct entry of \sim 100-500 eV electrons results in energy deposition at 200-
 46 300 km altitude where ambient electron temperatures can remain elevated, due to min-
 47 imal collisional loss to the rarefied neutral atmosphere, and large field-aligned flows can
 48 be initiated (Su et al., 1999; Zettergren et al., 2007). These upflows are likely further en-
 49 ergized by broadband extremely low frequency (BBELF) waves, also common in the cusp
 50 (Strangeway et al., 2005; Kintner et al., 1996)

51 Poleward moving auroral forms (PMAFs) are quasi-periodic sequences of poleward
 52 propagating auroral features, likely associated with pulsed reconnection at the magne-
 53 topause (Moen et al., 2004, and references therein). Cusp PMAFs are likely to have a
 54 direct impact on ionospheric plasma escape because of the highly transient nature of the
 55 associated soft particle precipitation (Su et al., 1999; Moen et al., 2004). Each PMAF
 56 may be comprised of smaller sub-arc structures (e.g. Skjaeveland et al., 2011), with spa-
 57 tial extents down to 100 m, that may play some role in variable ionospheric responses.
 58 PMAF sequences typically have repetition rate between 2-15 minutes with an average
 59 of \sim 8 minutes (e.g. Fasel, 1995; Sandholt et al., 1993). Each successive PMAF deposits
 60 energy into the local ionosphere, which has been altered to a varying degree by the pre-
 61 vious PMAF, resulting, in principle, in a cumulative, complex upflow effect. Because plasma
 62 is being extracted (via upflow) from \sim 250 km altitudes the response of the ionosphere
 63 to successive PMAFs depends in a complicated way on its past time history. Hence, the
 64 variable dwell time of PMAFs, coupled with hysteresis, has the potential to create al-
 65 titude, latitude, and temporal dependence in upflow responses - features that are not well-
 66 explored.

67 Previous ionospheric modeling studies (e.g. Wu et al., 1999; Burleigh & Zettergren,
 68 2017) and comparisons against observations (e.g. Sanchez & Strømme, 2014) have demon-
 69 strated that ionospheric sources of plasma to the topside (controlled by low-altitude heat-
 70 ing and dynamics) can regulate outward ion fluxes. Most upflow studies examine the “step-
 71 response” of the ionosphere, by using a fixed precipitation input having some “ramp-up”

72 time scale or “on-off” paradigm (e.g. Sadler et al., 2019) - a sensible approach but one
 73 that cannot account for situations with complicated time-variable forcing. Few studies
 74 have attempted to address the time-dependent forcing effects of a realistically moving
 75 source or sequence of sources on upflows (e.g. Zettergren et al., 2014). Global models and
 76 single-beam radar experiments do not spatially or temporally resolve important local-
 77 scale, fast time-scale features associated with ion outflow - e.g. individual discrete arcs
 78 (0.5 - 10 km scales).

79 Realistic upflow forcing (i.e., source combinations and timing consistent with ob-
 80 servations during geophysically significant events) has not been properly characterized
 81 via modeling or observations, yet it is clearly of significance to outflow. Driving models
 82 with inputs based on observations (rather than specified in an ad hoc manner) should
 83 allow for a more accurate understanding of the duration and location of upflows. This
 84 study examines the cumulative spatial and temporal effects of a sequence of PMAFs driv-
 85 ing ionospheric field-aligned upflow, downflow, and potentially outflow as observed dur-
 86 ing the Rocket Experiment for Neutral Upwelling 2 (RENU2) sounding rocket campaign.
 87 The primary goal of this study is to assess the effects of realistic transient vs. steady cusp-
 88 type forcing on low-altitude upflow. This will provide a better understanding of the er-
 89 rors in modeling upflow with poorly resolved energy inputs, and provide realistic expec-
 90 tations for events.

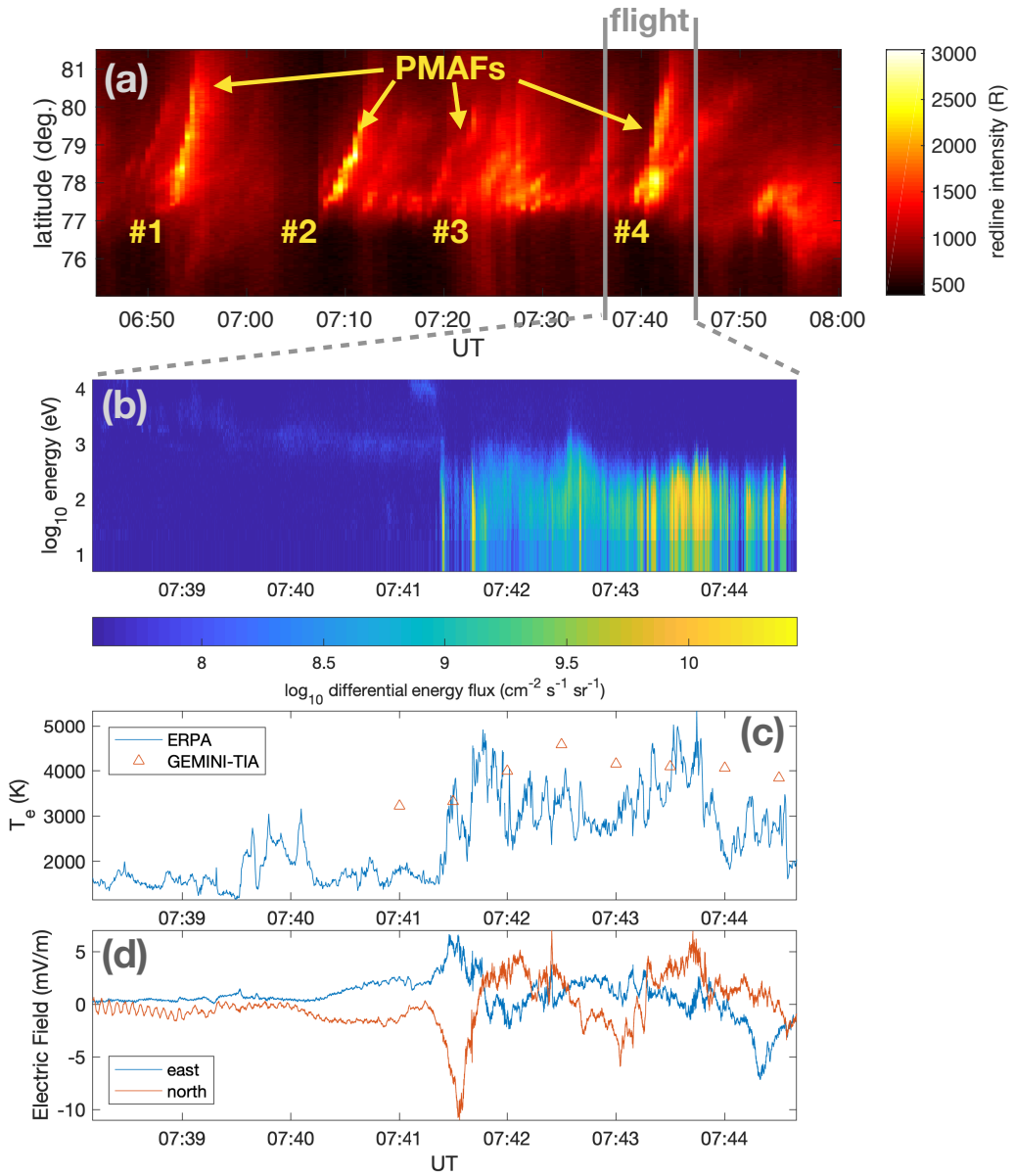
91 2 Data Motivating Modeling Efforts

92 The RENU2 sounding rocket was launched from the Andøya rocket range on De-
 93 cember 13, 2015 at 7:34 UT into the fourth of a series of PMAFs. These PMAFs were
 94 observed from \sim 6:45 UT onwards through the time of flight, indicating cusp aurora, by
 95 the University of Oslo all-sky imager at Longyearbyen (LYR) (data can be found at <http://tid.uio.no/plasma/aurora/>). In general, the PMAFs exhibited northward movement
 96 with a speed of \sim 1 km/s and latitudinal width of \sim 0.6° (as discerned from redline im-
 97 ager data, Figure 1a). Each PMAF displays unique deviations from this general pattern.

98 RENU2 in situ electron precipitation measurements in Figure 1b show passage through
 99 the cusp in the latter part of the flight (7:41:20 UT onwards) - characterized by soft (<
 100 300 eV) particle precipitation, which will deposit energy at \geq 200 km altitude, exciting
 101 strong 630 nm emission (panel a) and heating the ambient ionospheric electrons. ERPA
 102 data (Frederick-Frost et al., 2007) from RENU2 are shown in Figure 1c and illustrate
 103 a clear correlation between elevated electron temperatures and the softer particle pre-
 104 cipitation. DC electric field measurements from the COWBOY instrument (Lundberg,
 105 Kintner, Powell, & Lynch, 2012; Lundberg, Kintner, Lynch, & Mella, 2012, and refer-
 106 ences therein), Figure 1d, are small but show an enhancement just equatorward of the
 107 cusp/PMAF. These measurements, when compared to the speed of this PMAF, suggest
 108 that the PMAF was not locked into the slower background convection; a somewhat un-
 109 usual situation (e.g. Kozlovsky & Kangas, 2002). A more comprehensive description and
 110 analysis of the data summarized in Figure 1 is given in Lessard et al. (2019). Here we
 111 focus on only the basic features necessary to set up a modeling study of *transient behav-
 112 ior*. Collectively, the information shown in Figure 1a, b, and d, are used as inputs to drive
 113 the Geospace Environment Model of Ion-Neutral Interactions with Transverse Ion Ac-
 114 celeration (GEMINI-TIA) ionospheric model.

115 3 Ionospheric Model

116 GEMINI-TIA (described in detail in Burleigh & Zettergren (2017)) is the 2D, multi-
 117 fluid, ionospheric model used for this study. GEMINI-TIA solves the nonlinear equations
 118 for conservation of mass, momentum, parallel energy, and perpendicular energy for six
 119 ion species relevant to the *E* and *F* regions and topside ionosphere (O^+ , NO^+ , N_2^+ , O_2^+ ,
 120 N^+ , and H^+). This fluid description is coupled to a quasi-static solution for auroral and



99 **Figure 1.** Normalized, along-trajectory brightness measurements from the imager at LYR
 100 (panel a), in situ precipitation measurements in the form of characteristic energy and total en-
 101 ergy flux (panel b) and the in situ DC electric field (panel d) are processed and used as model
 102 inputs. The in situ electron temperature measurements (panel c) can be compared to model
 103 results.

127 neutral dynamo electric currents. GEMINI-TIA includes the effects of precipitating elec-
 128 trons on the ambient ionospheric plasma, including ionization and thermal electron heating - necessary to capture *F* region and topside upflow. GEMINI-TIA further includes
 129 a parameterization of transverse heating by BBELF waves and parallel ion inertial ef-
 130 fects necessary for simulating high-speed plasma upflows.
 131

132 Inputs for GEMINI-TIA include topside ionospheric potential, electron precipita-
 133 tion, power spectral density from BBELF waves, and neutral winds (Burleigh et al., 2018).
 134 For this study, GEMINI-TIA is initialized only with data-inspired precipitation and DC
 135 electric field values to mimic the effects of the observed PMAFs. The model utilizes a
 136 non-uniform tilted-dipole grid (Huba et al., 2000) with a resolution of $\sim 4 \times 12$ km (horizontal \times vertical)
 137 in the *E* region and increases to a resolution of $\sim 6 \times 15$ km in the topside. The grid's geo-
 138 physical location is set to encompass the rocket trajectory. The model uses an adaptive
 139 time step to ensure stability, typically ~ 1.4 s for this type of grid.

140 In situ particle precipitation and DC electric field measurements (Figure 1b and
 141 d, respectively) are used as reference for selecting representative input values for the model.
 142 Specifically, a northward DC electric field of 8 mV/m, a total energy flux of 0.75 mW/m²,
 143 and a characteristic energy of 100 eV are used as the energy inputs driving the model.
 144 For each time step, the brightness measurement from the ground based all-sky imager
 145 at Longyearbyen (LYN) was smoothed using a Gaussian-weighted moving average with
 146 a fixed window length of 50 points to retain the fundamental shape of the PMAFs in the
 147 keogram while suppressing measurement noise. The total energy flux and the DC elec-
 148 tric field are multiplied by the normalized, and smoothed, brightness measurements (Fig-
 149 ure 3a) to control where, when, and at what relative strength the aurora is modeled. The
 150 data are then linearly interpolated over time to increase the temporal resolution from
 151 a 30 second cadence to a 5 second cadence to facilitate model use. Preserving the unique
 152 and detailed energy signature for each PMAF is beyond the scope of this paper but may
 153 be a future focus. The brightness weighted, constant energy drivers are implemented to
 154 allow for the impacts of the variability of the PMAF sequence to be the focus of this study.

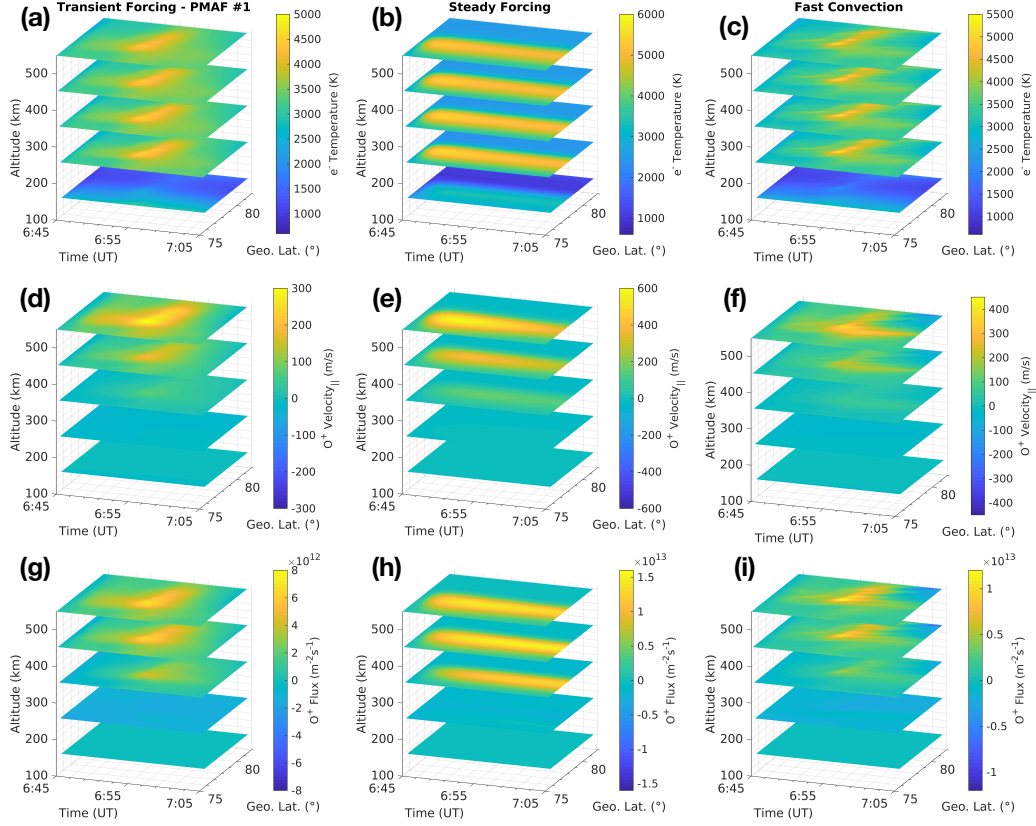
155 To illustrate the impact of background convection, a second simulation has been
 156 run that uses the same inputs above and a brightness weighted eastward DC electric field
 157 of 50 mV/m. This generates a local background convection approximately equivalent to
 158 the PMAF speed (~ 1 km/s). We also run a third simulation assuming steady forcing,
 159 to contrast with the runs with transient forcing. This third simulation uses total energy
 160 flux (0.75 mW/m²) and characteristic energy (100 eV) which are applied constantly for
 161 20 minutes using a latitudinal Gaussian envelope, centered on $\sim 77^\circ$, with a half-width
 162 of $\sim 0.6^\circ$ to create latitudinal structure.

163 4 Ionospheric Response to a Sequence of PMAFs

164 4.1 Transient vs. Steady Forcing

165 Three simulations to study transient vs. steady cusp-type forcing on low-altitude
 166 upflow are presented in this section. Cusp auroral precipitation increases electron den-
 167 sities and temperatures, hence pressure, throughout the *F* region and topside ionosphere.
 168 The electron pressure increase results in a stronger ambipolar electric field which enhances
 169 the upward field-aligned flow of plasma (Su et al., 1999). The electron temperature, O⁺
 170 field-aligned velocity, and O⁺ flux from 6:45 to 7:05 UT are shown in Figure 2 for each
 171 simulation (Transient Forcing - PMAF #1 vs. Steady Forcing vs. Fast Convection).

172 The 100 eV soft precipitation, within the steady forcing simulation, quickly elevates
 173 electron temperatures from ~ 2000 K to 6000 K (Figure 2b) at 76° and, through auro-
 174 ral ionization, creates more *F* region O⁺. As local ion densities increase, the energy de-
 175 posited into the *F* region from the auroral precipitation is distributed amongst/acts on
 176 an increasing ion population resulting in slightly less apparent electron heating as the



182 **Figure 2.** From the top down, the electron temperature, O^+ field aligned velocity, and the
 183 O^+ flux at five altitudinal slices (150, 250, 350, 450, 550 km) from 6:45 to 7:05 UT for the
 184 realistic transient forcing (left column), steady forcing (center column), and fast convection
 185 (right column) simulations. Note: Colorbar ranges are not identical.

177 event proceeds. The O^+ velocity in the topside is driven to >600 m/s within ~ 2 minutes
 178 and then tapers off as more material is pushed upwards, counteracting the initial
 179 pressure gradient (panel e). The O^+ flux during this simulation remains mostly constant
 180 due to the fact that there are more ions at higher altitudes which approximately coun-
 181 terbalances the decrease in drift speed with time as the event progresses (panel h).

186 For comparison, the transient forcing simulation utilizes just the first PMAF (#1)
 187 that occurred during the same time window (6:45–7:05 UT) (see Figure 1a). The PMAF
 188 dwells in the same latitudinal region ($\sim 78^\circ$), increasing the local ionospheric response
 189 (i.e. greater ion fluxes, stronger field aligned ion velocities, and larger temperatures), un-
 190 until $\sim 6:50$ UT when there is brightening/northward elongation and motion. The motion
 191 northward then results in a relatively smaller amount of energy (as compared to the steady
 192 forcing simulation) being deposited in any localized region. The normalized-brightness
 193 data provides a realistic spatiotemporal variability in the energy input location and strength,
 194 as seen in the structured response in Figure 2a, d, and g. Increasing the background con-
 195 vection to be roughly equivalent to the PMAF speed results in a stronger structured re-
 196 sponse (Figure 2c, f, and i) from the local plasma staying within the moving energiza-
 197 tion region longer and additional frictional heating.

198 The steady cusp-type forcing generates an O^+ response almost twice the intensity
 199 of the realistic transient forcing. Integrating the flux over time and space, the total num-

ber of O^+ ions transported by the steady cusp-type forcing is 3.3×10^{16} at 1000 km over the course of the simulation. By comparison, the transient forcing - PMAF #1 simulation has a total transport of 1.9×10^{16} O^+ ions at 1000 km and the fast convection simulation generates 3.0×10^{16} ions at 1000 km. While the northward propagation of the PMAF allows for more spatial area to be energized, the total amount of energy input into a given area can be less. Using constant forcing, or a long duration “on-off” mechanism, to represent PMAFs, has the potential to severely over-estimate ionospheric responses.

4.2 Effects of a Sequence of PMAFs

Using the full observed PMAF sequence (6:45 to 8:00 UT) generates a structured ion response in the model. The first PMAF from $\sim 6:47$ to 7:04, sweeps poleward through the local ionosphere and lofted ions upwards. The first PMAF to pass through the region generates the strongest flows. There are only a few minutes of “rest time” between the first and second PMAF for the ionosphere to relax back towards a quiescent state and begin to downflow (this is relatively short compared to the time required to establish a relatively steady ion upflow response (e.g. Burleigh & Zettergren, 2017)). The second PMAF, from $\sim 7:07$ to 7:18 UT, deposits energy at approximately the same latitudes as the first PMAF which increases O^+ densities at higher altitudes, as shown in Figure 3d. The third PMAF, from $\sim 7:18$ to 7:38 UT is not as strong but has a longer duration. The fourth PMAF, from $\sim 7:38$ to 7:51 UT, is the PMAF the rocket flew through. The cumulative effects of this series of PMAFs can be seen in the large increase in O^+ densities at even higher altitudes (panel e).

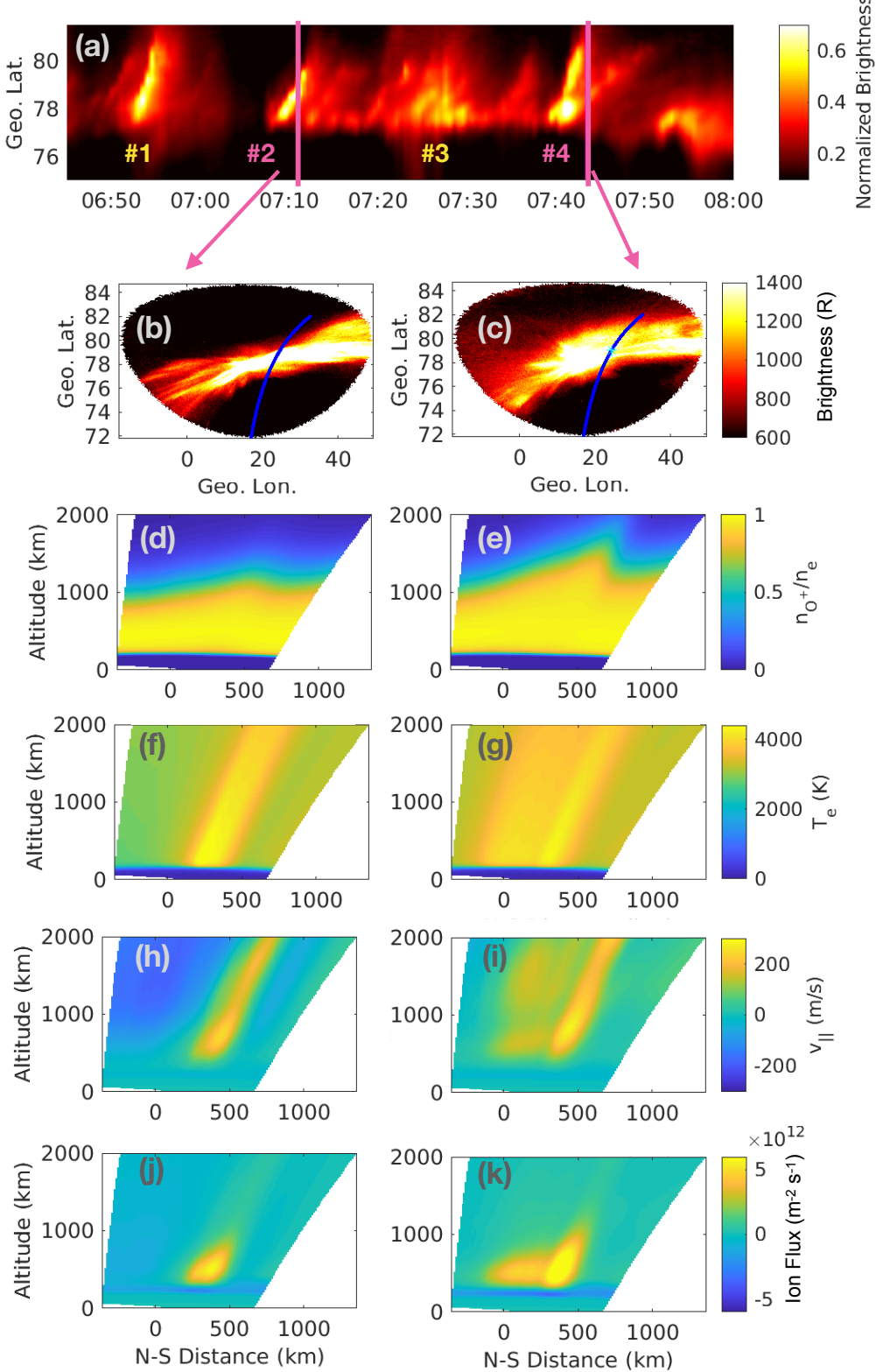
PMAF motions, and changes in intensity, generate periods of significant latitudinal differences in the ionospheric state. For example, during the second PMAF at 7:11 UT, auroral precipitation increases electron temperatures and drives upflow between ~ 77 - 78° (Figure 3f and h respectively). In contrast, the northernmost modeled latitudes ($> 79^\circ$) at this time have not been re-visited by auroral activity and show downflow (panel h). PMAF dwell time in a latitudinal region determines the amount of ion flux generated (panel j).

Only local, medium scale downflows are generated in this simulation. Smaller sub-arc (spatial) scale downflows are often observed by sounding rockets (Lynch et al., 2007; Fernandes et al., 2016). These sub-arc scale structures are not captured here potentially due to the structure size being below the resolution of the simulation or smoothing applied to model inputs removed fine scale details responsible for driving the downflows. However, this simulation does illustrate a scenario under which downflows occur, i.e. strong forcing at local spatial and temporal scales.

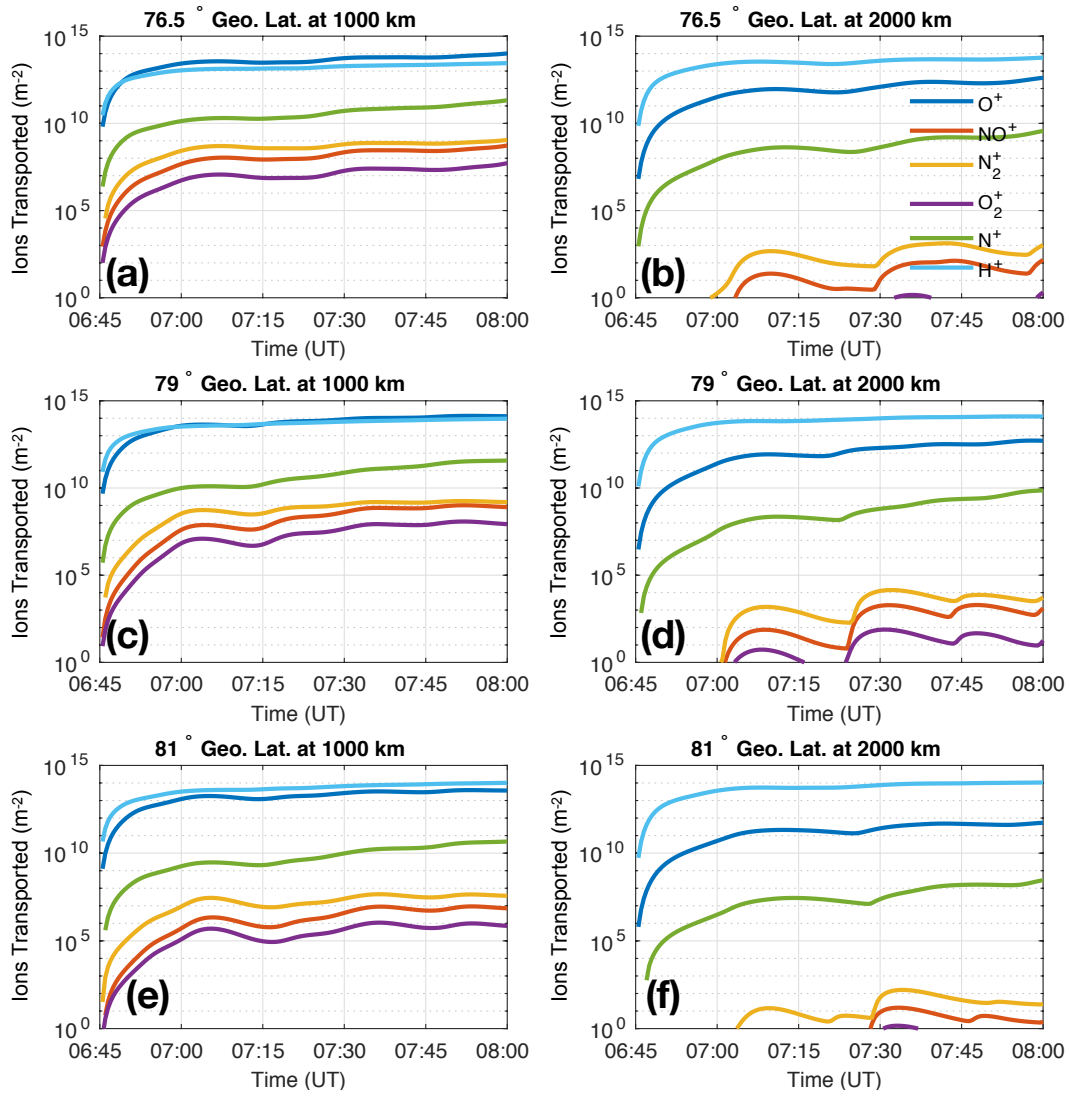
As an additional example of the dynamic response to PMAF motions, latitudes $> 79^\circ$ that previously contained downflow after PMAF #1, show upflow (panel i) at 7:43:30, as PMAF #4 (panel c) passes through the region. The latitudinal extent of the PMAF motion has elevated electron temperatures over a broad region (panel g). Effects of time history are evident as a stronger part of the PMAF has just passed through the region (see the brighter region just to the left of the second magenta line in Figure 3a) resulting in, cumulatively, more O^+ lofted to higher altitudes (panel e). The ion flux at this time is larger as well (panel k).

When the RENU2 sounding rocket (Figure 3c, cyan star) is within the fourth PMAF the electron temperatures (Figure 1c, blue line) fluctuate between 2500 and 5000 K from $\sim 7:41:20$ to $\sim 7:44:00$. The modeled electron temperatures, at the rocket’s location, fall within this range (Figure 1c, orange triangles) and provide a point of verification for this method of modeling PMAFs.

The variable dwell time of PMAFs at a latitudinal region impacts the ion flux generated there at high altitudes. At 1000 km, the upflow takes ~ 7 minutes to reach this



221 **Figure 3.** Modeled ionospheric parameters from PMAF #2 at 7:11:00 (left column) and
 222 PMAF #4 at 7:43:30 UT (right column). These times are indicated by the magenta vertical lines
 223 in panel a. The all-sky imager brightness (panels b and c) are overlaid with the rocket trajectory
 224 (and keogram trace line) in blue. The model uses a tilted-dipole grid as seen in panels d-k.



252 **Figure 4.** Cumulative number of particles per unit area (transport) for each ion specie pass-
 253 ing through 1000 km and 2000 km at three separate latitudes. The results from a control simu-
 254 lation, without any PMAFs (i.e. including only ambient transport effects), have been subtracted to
 255 highlight PMAF driven transport.

258 altitude (difference in time between the end of the brightness of the PMAF and the cor-
 259 responding peak in transport at this altitude in Figure 4). At 2000 km, it takes \sim 11 min-
 260 utes for ion upflow to reach this altitude. Increasing transport over time is due to up-
 261 flow and decreasing transport is due to downflow. At 76.5° , PMAFs 1 and 3 have the
 262 greatest impact on the transport; PMAFs 2 and 4 do not provide significant precipita-
 263 tion this far south. This is seen in the two peaks in transport at both 1000 and 2000 km
 264 in Figure 4a and b. At 79° (panels c and d) and 81° (panels e and f), all four PMAFs
 265 influence this region (minimal influence from PMAF 2 at 81°). The dwell time of PMAF
 266 activity around 81° is shorter than at 79° so less material reaches 2000 km.

267 There is a transport response time difference between the ion species at these al-
 268 titudes. For example, the first peak in transport at 1000 km, at 81° (Figure 4e), is reached
 269 by O^+ at 7:05:00, N^+ at 7:05:30, NO^+ at 7:06:00, N_2^+ at 7:05:30, and O_2^+ at 7:05:30; a
 270 minute spread in response time. H^+ at this altitude and latitude does not have a dis-
 271 tinct peak for comparison; the transport continues to increase over time. The response
 272 time differences become more pronounced by the second PMAF, which is from \sim 7:07
 273 to 7:18 UT. The species dependent delay at which the ion species changes from down-
 274 flowing to upflowing is at 7:14:00 for O^+ , 7:14:00 for N^+ , 7:16:00 for NO^+ , 7:16:30 for
 275 N_2^+ , and 7:16:30 for O_2^+ for this PMAF. The overall transition from downflow to upflow
 276 for all ion species occurs over a period of 2 minutes and 30 seconds.

277 5 Conclusions and Future Work

278 In this study we demonstrate a data-representative (as opposed to data-driven) mod-
 279 eling approach to incorporate brightness from all-sky imagers as a constraint for auro-
 280 ral ionospheric model inputs. This method allows for realistic forcing that is not cap-
 281 tured with a traditional “on-off” descriptions of PMAFs. There is agreement between
 282 the electron temperatures measured in situ by the rocket and the modeled electron tem-
 283 peratures along the rocket trajectory during PMAF #4 when the rocket was in flight (see
 284 Figure 1c) indicating that this method works well for local-scale features.

285 Comparing the steady forcing simulation to PMAF #1, the basic physical processes
 286 in play are the same; auroral precipitation elevates electron densities and temperatures
 287 resulting in an enhanced ambipolar electric field which drives ion upflow. The steady forcing
 288 simulation shows upflow confined to latitudes (\sim 75–78 $^\circ$) where the energy inputs as-
 289 sociated with auroral precipitation are largest. The PMAF simulation, on the other hand,
 290 shows large latitudinal and temporal variation of ion upflow and electron temperature.
 291 The total O^+ transported through 1000 km, due to the steady forcing, is approximately
 292 twice that generated by PMAF #1, which generated the strongest upflows from the PMAF
 293 sequence and still 10% greater than the fast convection simulation.

294 Using the full PMAF sequence generates significant spatiotemporal variation of field-
 295 aligned ion velocities and fluxes within the model. The variable dwell time of the PMAFs
 296 in any given latitudinal region impacts the ion flux generated there at high altitudes. For
 297 example, not all PMAFs had the same latitudinal extent, two did not reach as far south
 298 as 76.5° so that latitudinal region received less energy. The dwell time of each PMAF
 299 at higher latitudes, for example at 81° , is shorter than at 79° so less ionospheric mate-
 300 rial is driven to 2000 km. There is also an ion species dependence in the response time
 301 where the heavier molecular ions are slower to respond. By the second PMAF, there is
 302 a 2 minute 30 second spread in response as downflows are driven to upflows.

303 While soft electron precipitation is itself insufficient to accelerate ions to escape ve-
 304 locities, source populations available for higher-altitude energization processes are greatly
 305 increased. Plans for future work include a characterization of transverse energization ef-
 306 fects. The transient nature of PMAFs may affect the conversion of upflow to outflow via
 307 BBELF transverse ion acceleration.

308 **Acknowledgments**

309 MB was supported by NSF CAREER grant AGS-1255181 and NASA grant 80NSSC17K0015,
 310 MZ by NSF CAREER grant AGS-1255181, and ML by NASA grant 80NSSC17K0015.
 311 Support was provided at the University of New Hampshire by NASA award NNX13AJ94G,
 312 at Dartmouth College by NASA award NNX13AJ90G, and at Cornell University by NASA
 313 award NNX13AJ91G. JM received funding from the Research Council of Norway grant
 314 275653.

315 RENU2 data are available at NASA's Space Physics Data Facility (SPDF, spdf.gsfc.nasa.gov). University of Oslo all-sky imager data are available at <http://tid.uio.no/plasma/aurora>. Model results (doi:10.7302/pcrt-dj64) are archived in Deep
 316 Blue Data (<https://deepblue.lib.umich.edu/data>).

319 **References**

320 Burleigh, M. R., Heale, C. J., Zettergren, M. D., & Snively, J. B. (2018). Modulation
 321 of low-altitude ionospheric upflow by linear and nonlinear atmospheric gravity
 322 waves. *Journal of Geophysical Research: Space Physics*, 123(9), 7650-7667. doi:
 323 10.1029/2018JA025721

324 Burleigh, M. R., & Zettergren, M. D. (2017). Anisotropic fluid modeling of iono-
 325 spheric upflow: Effects of low-altitude anisotropy and thermospheric winds. *Journal*
 326 *of Geophysical Research: Space Physics*. doi: 10.1002/2016JA023329

327 Chappell, C. R. (1988). The terrestrial plasma source: A new perspective in solar-
 328 terrestrial processes from dynamics explorer. *Reviews of Geophysics*, 26(2), 229-
 329 248. doi: 10.1029/RG026i002p00229

330 Fasel, G. J. (1995). Dayside poleward moving auroral forms: A statistical study.
 331 *Journal of Geophysical Research: Space Physics*, 100(A7), 11891-11905. doi: 10
 332 .1029/95JA00854

333 Fernandes, P. A., Lynch, K. A., Zettergren, M., Hampton, D. L., Bekkeng, T. A.,
 334 Cohen, I. J., ... Powell, S. P. (2016). Measuring the seeds of ion outflow:
 335 Auroral sounding rocket observations of low-altitude ion heating and circula-
 336 tion. *Journal of Geophysical Research: Space Physics*, 121(2), 1587-1607. doi:
 337 10.1002/2015JA021536

338 Frederick-Frost, K. M., Lynch, K. A., Kintner, P. M., Klatt, E., Lorentzen, D.,
 339 Moen, J., ... Widholm, M. (2007). Sersio: Svalbard eiscat rocket study of ion
 340 outflows. *J. Geophys. Res.*, 112.

341 Gloeckler, G., & Hamilton, D. C. (1987). Ampte ion composition results. *Physica*
 342 *Scripta*, 1987(T18), 73. doi: 10.1088/0031-8949/1987/T18/009

343 Hamilton, D. C., Gloeckler, G., Ipavich, F. M., Stedemann, W., Wilken, B., &
 344 Kremser, G. (1988). Ring current development during the great geomagnetic
 345 storm of february 1986. *Journal of Geophysical Research: Space Physics*, 93(A12),
 346 14343-14355. doi: 10.1029/JA093iA12p14343

347 Huba, J. D., Joyce, G., & Fedder, J. A. (2000). Sami2 is another model of the iono-
 348 sphere (sami2): A new low-latitude ionosphere model. *Journal of Geophysical Re-*
 349 *search: Space Physics*, 105(A10). doi: 10.1029/2000JA000035

350 Hultqvist, B., Øieroset, M., Paschmann, G., & Treumann, R. (1999). Magneto-
 351 spheric plasma sources and losses. *Space Sci. Rev.*, 88.

352 Kintner, P. M., Bonnell, J., Arnoldy, R., Lynch, K., Pollock, C., & Moore, T.
 353 (1996). SCIFER-Transverse ion acceleration and plasma waves. *Geophys. Res.*
 354 *Lett.*, 23, 1873-1876.

355 Kistler, L. M., Mouikis, C., Mbius, E., Klecker, B., Sauvaud, J. A., Rme, H., ...
 356 Balogh, A. (2005). Contribution of nonadiabatic ions to the cross-tail current
 357 in an o+ dominated thin current sheet. *Journal of Geophysical Research: Space*
 358 *Physics*, 110(A6). doi: 10.1029/2004JA010653

359 Kozlovsky, A., & Kangas, J. (2002). Motion and origin of noon high-latitude pole-
 360 ward moving auroral arcs on closed magnetic field lines. *Journal of Geophysical*
 361 *Research: Space Physics*, 107(A2). doi: 10.1029/2001JA900145

362 Kozyra, J. U., Shelley, E. G., Comfort, R. H., Brace, L. H., Cravens, T. E., & Nagy,
 363 A. F. (1987). The role of ring current $o+$ in the formation of stable auroral red
 364 arcs. *Journal of Geophysical Research: Space Physics*, 92(A7), 7487-7502. doi:
 365 10.1029/JA092iA07p07487

366 Lessard, M. R., F., B., S., B., Cohen, I., D. Kenward, N. G., Clemons, J. H., ...
 367 Yeoman, T. (2019). Overview of the Rocket Experiment for Neutral Upwelling
 368 Sounding Rocket 2 (RENU2). *Geophys. Res. Lett.* (submitted)

369 Lundberg, E. T., Kintner, P. M., Lynch, K. A., & Mella, M. R. (2012). *Multi-*
 370 *payload measurement of transverse velocity shears in the topside ionosphere*
 371 (Vol. 39). doi: 10.1029/2011GL050018

372 Lundberg, E. T., Kintner, P. M., Powell, S. P., & Lynch, K. A. (2012). *Multi-*
 373 *payload interferometric wave vector determination of auroral hiss* (Vol. 117). doi:
 374 10.1029/2011JA017037

375 Lynch, K. A., Semeter, J. L., Zettergren, M., & Kinter, P. (2007). Auroral ion out-
 376 flow: Low altitude energization. *Ann. Geophys.*, 25.

377 Moen, J., Oksavik, K., & Carlson, H. C. (2004). On the relationship between ion up-
 378 flow events and cusp auroral transients. *Geophys. Res. Lett.*, 31, 11808.

379 Moore, T. E., & Delcourt, D. C. (1995). The geopause. *Reviews of Geophysics*,
 380 33(2), 175-209. doi: 10.1029/95RG00872

381 Moore, T. E., Fok, M.-C., Chandler, M. O., Chappell, C. R., Christon, S. P., Del-
 382 court, D. C., ... Slinker, S. (2005). Plasma sheet and (nonstorm) ring current
 383 formation from solar and polar wind sources. *Journal of Geophysical Research:*
 384 *Space Physics*, 110(A2).

385 Moore, T. E., & Horwitz, J. L. (2007). Stellar ablation of planetary atmospheres.
 386 *Reviews of Geophysics*, 45, 1944-9208.

387 Nösé, M., Taguchi, S., Hosokawa, K., Christon, S., McEntire, R., Moore, T., & Col-
 388 lier, M. (2005). Overwhelming $o+$ contribution to the plasma sheet energy density
 389 during the october 2003 superstorm: Geotail/epic and image/lena observations.
 390 *Journal of Geophysical Research: Space Physics*, 110(A9).

391 Orsini, S., Candidi, M., Stokholm, M., & Balsiger, H. (1990). Injection of iono-
 392 spheric ions into the plasma sheet. *Journal of Geophysical Research: Space*
 393 *Physics*, 95(A6), 7915-7928. doi: 10.1029/JA095iA06p07915

394 Sadler, F. B., Lessard, M., & Otto, A. (2019). Effects of periodic precipitation on ion
 395 upflow and neutral upwelling. *Geophys. Res. Lett.* (submitted)

396 Sanchez, E. R., & Strømme, A. (2014). Incoherent scatter radar-fast satellite com-
 397 mon volume observations of upflow-to-outflow conversion. *Journal of Geophysical*
 398 *Research: Space Physics*, 119(4), 2649-2674. doi: 10.1002/2013JA019096

399 Sandholt, P., Moen, J., Opsvik, D., Denig, W., & Burke, W. (1993). Auroral event
 400 sequence at the dayside polar cap boundary: Signature of time-varying solar wind-
 401 magnetosphere-ionosphere coupling. *Advances in Space Research*, 13(4), 7 - 15.
 402 doi: [https://doi.org/10.1016/0273-1177\(93\)90305-U](https://doi.org/10.1016/0273-1177(93)90305-U)

403 Shay, M. A., Drake, J. F., Swisdak, M., & Rogers, B. N. (2004, May). The scaling of
 404 embedded collisionless reconnection. *Physics of Plasmas*, 11, 2199-2213. doi: 10
 405 .1063/1.1705650

406 Skjaeveland, A., Moen, J., & Carlson, H. C. (2011). On the relationship between
 407 flux transfer events, temperature enhancements, and ion upflow events in the cusp
 408 ionosphere. *Journal of Geophysical Research: Space Physics*, 116(A10).

409 Strangeway, R. J., Ergun, R. E., Su, Y. J., Carlson, C. W., & Elphic, R. C. (2005).
 410 Factors controlling ionospheric outflows as observed at intermediate altitudes. *J.*
 411 *Geophys. Res.*, 110.

412 Su, Y., Caton, R., Horwitz, J., & Richards, P. (1999). Systematic modeling of

413 soft-electron precipitation effects on high-latitude f region and topside ionospheric
414 upflows. *Journal of geophysical research*, 104, 153–163.

415 Varney, R. H., Wiltberger, M., Zhang, B., Lotko, W., & Lyon, J. (2016). Influence
416 of ion outflow in coupled geospace simulations: 1. physics-based ion outflow
417 model development and sensitivity study. *Journal of Geophysical Research: Space
418 Physics*, 121(10), 9671–9687. doi: 10.1002/2016JA022777

419 Welling, D., André, M., Dandouras, I., Delcourt, D., Fazakerley, A., Fontaine, D., ...
420 Yau, A. (2015). The earth: Plasma sources, losses, and transport processes. *Space
421 Science Reviews*, 192(1-4), 145–208.

422 Wu, X.-Y., Horwitz, J. L., Estep, G. M., Su, Y.-J., Brown, D. G., Richards, P. G.,
423 & Wilson, G. R. (1999). Dynamic fluid-kinetic (dyfk) modeling of auroral
424 plasma outflow driven by soft electron precipitation and transverse ion heating.
425 *Journal of Geophysical Research: Space Physics*, 104(A8), 17263–17275. doi:
426 10.1029/1999JA900114

427 Young, D. T., Balsiger, H., & Geiss, J. (1982). Correlations of magnetospheric ion
428 composition with geomagnetic and solar activity. *Journal of Geophysical Research:
429 Space Physics*, 87(A11), 9077–9096. doi: 10.1029/JA087iA11p09077

430 Zettergren, M., Lynch, K., Hampton, D., Nicolls, M., Wright, B., Conde, M., ...
431 Powell, S. (2014). Auroral ionospheric f region density cavity formation and evo-
432 lution: Mica campaign results. *Journal of Geophysical Research: Space Physics*,
433 119(4), 3162–3178. doi: 10.1002/2013JA019583

434 Zettergren, M., Semeter, J., Blelly, P. L., & Diaz, M. (2007). Optical estimation of
435 auroral ion upflow: Theory. *J. Geophys. Res.*, 112.